Increased atmospheric river frequency slowed the seasonal recovery of Arctic sea ice in recent decades

Pengfei Zhang[1*], Gang Chen[2], Mingfang Ting[3], L. Ruby Leung[4], Bin Guan[5,6], Laifang Li[1]

[1] Department of Meteorology and Atmospheric Science, The Pennsylvania State University, University Park, PA, USA
[2] Department of Atmospheric and Oceanic Sciences, University of California, Los Angeles, CA, USA
[3] Lamont-Doherty Earth Observatory, Columbia University, Palisades, NY, USA
[4] Atmospheric Sciences and Global Change Division, Pacific Northwest National Laboratory, Richland, WA, USA
[5] Joint Institute for Regional Earth System Science and Engineering, University of California, Los Angeles, CA, USA
[6] Jet Propulsion Laboratory, California Institute of Technology, Pasadena, CA, USA

Initial submission, Feb. 21, 2022
Revision, July.30, 2022

[*] Corresponding author: Pengfei Zhang (pfz5053@psu.edu, zpengfei1006@gmail.com)

Abstract

In recent decades, Arctic sea ice coverage experienced a drastic decline in winter, when sea ice is expected to recover following the melting season. Using observations and climate model simulations, we found a robust frequency increase in atmospheric rivers (ARs, intense corridors of moisture transport) over Barents-Kara Seas and the neighboring central Arctic (ABK) in early winter. The extensive moisture carried by more frequent ARs has intensified surface downward longwave radiation and liquid rainfall, caused stronger melting of thin, fragile ice cover, and slowed the seasonal recovery of sea ice, contributing to the sea ice cover decline in ABK. A series of model ensemble experiments suggests that, in addition to a uniform AR increase in response to anthropogenic forcing, the contribution of tropical Pacific variability is indispensable in the observed Arctic AR changes. These findings have significant implications for understanding the rapidly changing Arctic hydroclimate and the cryosphere.

Recent decades have witnessed a rapid decline in Arctic sea ice during its winter ice-growing season[1], which raised concerns as Arctic sea ice changes may fuel severe winter storms in mid-latitude continents[2,3] and reshape the ecosystem and fisheries in the Arctic region[4,5]. Wintertime sea ice area (SIA) decline, especially in Barents-Kara Seas, has been attributed to atmospheric heat transport by poleward moisture fluxes[e.g., 6–8], while enhanced oceanic heat transport through Nordic Sea has aggravated ice thinning and ice volume decline[9–14].

The bulk of Arctic moisture import is driven by atmospheric rivers (ARs)[15]. ARs are long, narrow, and transient corridors of strong horizontal moisture transport, typically accompanied by a low-level jet ahead of the cold front of an extratropical cyclone[16]. Despite covering only 10% of the Earth's circumference in midlatitudes, ARs account for up to 90% of the poleward water vapor transport in these latitudes[17,18], playing a crucial role in the hydrological cycle[e.g.,15,19–21]. Recent studies reported that ARs can extend into the Arctic circle[22]. Thus, there is an emergent need to quantify the role of ARs in the recent Arctic climate change.

In polar regions, contrary to AR-induced snow accumulation in East Antarctica[23], the intense moisture and heat rapidly transported by ARs can exert a strong melting effect on the cryosphere, exemplified by ice sheet melt in Greenland[24] and West Antarctica[25], polynyas in the Weddell Sea[26], and the 2016-17 record low Arctic winter sea ice growth[22]. The physical processes relevant to AR-induced ice melt or impeded ice growth include (a) enhanced downward longwave radiation (DLW) due to extensive greenhouse effect of atmospheric water vapor, cloud radiative effect, and condensational heating release, (b) reduction or even sign change in turbulent heat fluxes from the ice surface, (c) insulating capacity of snow, and (d) melt energy carried by rainfall[e.g., 22,25–31].

In recent decades, more frequent ARs have been observed in Greenland and West Antarctica[24,25], which coincides with the poleward shift of ARs in a warming climate[32–34]. Our current knowledge of ARs' melting effect leads us to hypothesize that the Arctic AR increase (if it exists over the ice cover) contributes to winter sea ice decline. Although previous works have reported some AR-like plumes, such as moisture intrusions, can induce cold season sea ice loss[7,35], these synoptic systems only account for a small fraction (36-38%)[7] of Arctic moisture import compared to ARs (70-80%)[15] (see details in Supplementary Information, SI), and thus are less conclusive of the role of moisture transport in sea ice change. Furthermore, it is not completely understood to what extent human activities have contributed to the high-latitude AR changes in recent decades, affecting mitigation and adaptation planning of the rapidly changing Arctic water cycle.

This study builds on the established linkage between ARs and surface melting to examine the Arctic AR changes and their role in slowing down the winter Arctic sea ice recovery. We utilize a novel approach with a state-of-the-art climate model to quantify the contributions of anthropogenic forcing and the observed sea surface temperature (SST) variability over the tropical Pacific to Arctic AR changes. We also clarify the mechanisms behind the Arctic AR changes by separating

the dynamic (circulation change) and thermodynamic (moistening trend) effects. By focusing on ARs, we connect Arctic sea ice changes with phenomenologically understood extreme weather events (ARs) that account for a large portion of the Arctic moisture import.

ARs' melting effect on Arctic sea ice

The melting effect of Arctic ARs during the ice recovery season (Nov-Dec-Jan, NDJ) in 1979-2021 (Method) is shown in Fig.1. The negative SIC anomalies associated with AR occurrences indicate that ARs significantly retard ice growth throughout all marginal seas, including the Barents-Kara Seas, Hudson Bay, the Labrador Sea, the Baffin Bay, and the Chukchi-Bering Seas (Fig.1a). In the Atlantic sector where the newly formed ice cover is thin[9,10], more than half of the sea ice melting occurs during the AR "landfall" over the ice cover (Fig.1b), resulting in a reduction of ~5.5×10^4 km^2 sea ice area (SIA, Method) in the Barents-Kara Seas and the neighboring central Arctic to the north (ABK hereafter, the box in Fig.1b) within 3-4 days (Fig.1c).

The melting effect of ARs on sea ice is dominated by extensive DLW (partly contributed by clouds within ARs) from the intense warm water vapor carried by ARs, as well as AR-induced liquid rainfall (Fig.1c). The snowfall associated with ARs could cause an insulating effect at the sea ice surface, which inhibits ice growth over a much longer timescale (throughout the winter) in this region[30], while anomalies of surface turbulent fluxes rapidly decay after the AR landfall. In general, the AR occurrence is significantly correlated with negative SIA anomalies around the ABK area during the ice recovery season, which is robust throughout 1979-2021 (bars in Fig.1d).

Increased AR penetration into the Arctic and its impact on sea ice

In the past several decades, the Arctic has seen a significant increase in AR frequency in the early winter over ABK. This AR trend is robust across three observational datasets (Fig.2b, Fig.S1b-c), coinciding with the most pronounced winter sea ice loss in this region[e.g., 36]. In contrast, fewer ARs penetrate into inland Eurasia (60°-90°*E*) to the south of ABK.

Considering the strong melting effect of ARs, it is tempting to ask if the increased AR frequency could have contributed to the sea ice decline in the past several decades. The observed early winter SIC trend during 1979-2021 features a pronounced decline in the marginal seas, including the ABK, the Greenland Sea, the Labrador Sea, and the Chukchi Sea (Fig.S4a), where ARs exert the melting effect (Fig.1). Since the ARs' melting effect on the shrinkage of Arctic sea ice cover is manifested by DLW and liquid rainfall (Fig.1c), we show the trends of cumulated DLW and liquid rainfall associated with ARs in NDJ in Fig.3(a-b). As the frequency of Arctic ARs increases in the ABK region, the cumulated AR DLW is significantly intensified (Fig.3a), which is partly contributed by the enhanced cloud radiative effect (Fig.S5a). The proportional contribution of the cloud radiative effect to the cumulated AR DLW underscores the role of clouds in enhancing the AR-related DLW (Fig.S6).

The cumulated AR liquid rainfall, especially along the ice edge where the new ice cover forms, is greatly strengthened (Fig.3b), while the AR-induced snowfall changes are relatively small (Fig.S5b). In the marginal ice zone of ABK, the correlation between SIC and rainfall (-0.61) is even higher than that with DLW (-0.47) during ARs, indicating a strong sea ice melting effect due to AR-related liquid rainfall there. We also examine the above physical processes associated with ARs' melting effect in the coupled climate model experiment of PAC2 (see model experiments in Method, which are analyzed in the next section) in Fig.3(c, d) and Fig.S5(c). The AR-induced DLW and liquid rainfall significantly increase in ABK, consistent with that in observations. Given the above results, it is expected that the increased AR frequency could have enhanced the melting effect of ARs and therefore contributed to the sea ice decline in recent decades.

To quantify the role of ARs in sea ice change, we examine the SIA growth in ABK, defined as the cumulative sum of the daily anomalies of SIA tendency in NDJ, with and without the contribution from ARs (Method) (Figure 4). Since the Arctic winter surface temperature in the current climate is below the freezing point, it is expected that the general decline of sea ice in summer could lead to a faster thermodynamic ice growth in winter. At the same time, the ice thickness has thinned due to oceanic warming[11–14], and thinner ice grows faster[9,10]. Indeed, a significantly faster SIA growth in NDJ is seen without the ARs' impact (blue line in Fig.4). Along with AR frequency increase, the melting effect on thin, fragile ice cover is enhanced (red line in Fig.4), which partly offsets the fast thermodynamic SIA growth and results in a weak, insignificant positive trend in total SIA growth (black line in Fig.4). Thus, frequent ARs can prevent the sea ice from growing to the extent allowed by the freezing winter surface temperature. Based on the AR's melting effect on ABK SIA as shown by the red line in Fig.4, we calculate the ABK SIA reduction associated with 1% AR frequency, which on average is $-8.8(\pm0.6)\times10^4$ km^2 in NDJ (Method). Then, by projecting the SIA reduction corresponding to 1% AR frequency to the actual AR frequency trend, we estimate the enhancement of the melting effect due to AR frequency increase, which accounts for ~34(±2)% of the total SIA decline in NDJ (Fig.2b). Qualitatively similar results are found in the PAC2 simulations (dashed lines in Fig.4). The SIA growth with and without ARs clearly demonstrates that more frequent ARs slow the seasonal sea ice growth and therefore contribute to the SIA decline during the ice growing season.

Drivers of Arctic AR frequency trends

In order to examine the causes for the Arctic AR trends, we first analyze the Global Ocean Global Atmosphere (GOGA2) experiment, an atmosphere-only model ensemble using CAM6/CESM2 forced by historical SST/sea ice and radiative forcing, which includes both the anthropogenic forcing and observed natural variability. Despite the bias of excessive ARs in the Bering Sea, the increasing ARs in the ABK, the AR climatology and the land-sea contrast of the AR changes in the Eurasian sector, are well reproduced in GOGA2 (Fig.5a), suggesting that the model is capable of simulating the observed AR changes.

To identify the contribution of anthropogenic warming, we analyze the CESM2 Large Ensemble (LENS2), a coupled ocean-atmosphere-sea ice model forced by historical radiative forcing (Methods). The LENS2 ensemble mean, which corresponds to the model response to external radiative forcing, shows a uniform positive trend in AR frequency over the entire high latitudes (Fig.5b). The maximum AR increase in LENS2 is in inland Eurasia, in contrast to fewer ARs in observations and GOGA2 for this region (Fig.2a, Fig.5a-b). Note that LENS2 and GOGA2 use the same atmosphere model and radiative forcing, except that GOGA2 is forced by observed variability in SSTs while LENS2 has internally generated SST variations with suppressed internal variability in its ensemble mean. The distinct spatial patterns of AR trends between LENS2 and GOGA2 suggest a possible role of the different SST variations. Notably, although the model SST biases might contribute to the disagreement between the LENS2 ensemble mean and the observed or GOGA2 AR trends, some LENS2 members share high similarity with GOGA2 and are distinct from the ensemble mean (left column in Fig.S8), further supporting a possible role of internal variability in the modeled and observed AR trends.

To examine the role of the observed SST variability, we employ a "pacemaker" experiment (PAC2) same as LENS2, except that the tropical Pacific SSTa is nudged towards the observed variations (Methods). We focus on the tropical Pacific here as it is the region with the most prominent modes of natural climate variability, that can exert a stronger influence on the Arctic than any other ocean basins[37,38]. Figure 5(c) shows that PAC2 captures the significant AR increases around the ABK region with a spatial pattern similar to that of GOGA2. By comparing the spatial patterns of AR trends in PAC2 and LENS2, with the tropical Pacific SST variability being the only difference between the two, it can be inferred that the tropical Pacific influence is non-negligible and must be considered to fully understand the observed AR trends in the Arctic.

The PAC2 results are designed to represent the combined effects of anthropogenic warming and, at least partly, the observed tropical Pacific influence. Since these two factors are largely additive, the contribution of tropical Pacific variability can be obtained by calculating the differences between PAC2 and LENS2, as shown in Fig.5(d) (see Method for more detailed interpretation and caveats). The observed variability from the tropical Pacific increases the AR frequency in the eastern Arctic, especially north of the ABK region, while significantly fewer ARs are found in inland Eurasia (Fig.5d). These results suggest that tropical Pacific variability is indispensable to simulate the observed spatial pattern of AR changes in the Arctic and Eurasian high latitudes.

To further quantify the AR trends in ABK and the relative contributions of anthropogenic warming versus tropical Pacific influence, Fig.5(e) shows the uncertainties of the area-averaged AR trends for ABK in the three sets of model experiments. The 95% confidence interval of GOGA2 encompasses the observed trend, indicating that the model forced with anthropogenic forcing and historical SST can capture the observed AR trend. In contrast, the observed AR trend is outside the 95% confidence intervals of the anthropogenic change alone (LENS2) or the tropical Pacific

influence alone (PAC2-LENS2). This suggests that the observed AR change cannot be fully explained by either external forcing or tropical Pacific variability alone, but rather the combined effect of anthropogenic forcing and internal climate variability. Based on Fig. 5e, the tropical Pacific influence accounts for 38(±12)% of the AR changes in PAC2. Note that the fraction will depend on the model's equilibrium climate sensitivity, which at 5.3K in CESM2 is larger than the best estimated range of 1.5-4.5K[39]. It implies that the contribution of tropical Pacific SST variability could be even higher in reality.

Mechanisms for Arctic AR changes

We further examine the mechanisms of the AR trends over the high latitudes in 0°-110°*E* in the past few decades. Since water vapor transport is the product of wind and moisture content, the mechanisms for the AR changes in a warming climate can be roughly divided into the part due to trends in wind (dynamic effect) and atmospheric moisture content (thermodynamic effect, consistent with Clausius-Clapeyron relation)[e.g., 34]. The decomposition of the two parts (See Methods for details) is shown in Fig.6. In observations, the AR increase in ABK is dominated by the thermodynamic effect, while the fewer ARs in west Eurasia are explained by the dynamic effect (Fig.6a-c). The thermodynamic AR increases in the Arctic are consistent with the increase in the atmosphere's water holding capacity due to fast Arctic warming, which supports increased AR frequency observed in the Arctic in recent decades. This is distinct from the high latitude AR increases observed in the Southern Hemisphere, which is dominated by the poleward shifted midlatitude jet, thus a dynamic effect[33]. The dynamical AR decrease in west Eurasia may be related to more persistent Ural blocking in recent decades[40], which suppresses cyclonic AR circulation. These land-sea contrasts in AR changes can also be seen in GOGA2 and PAC2, both, at least partly, constrained by the observed tropical Pacific variability (Fig.6 d-f, j-l). In fact, the tropical Pacific SSTa nudged to observations in the otherwise free running PAC2 experiment can produce a tropical Pacific-Arctic teleconnection, contributing to a warm Arctic[37,41]. This warming induced by tropical Pacific variability in combination with anthropogenic forcing favors more frequent ARs in the Arctic, which is well captured by GOGA2 and PAC2 (Fig.6 f, l).

In contrast, there is a weak dynamical contribution and a strong thermodynamic increase in inland west Eurasia in the ensemble mean of LENS2 (Fig.6 h, i), leading to the maximum AR increase over west Eurasia (Fig.6g and Fig.5b). These differences between the LENS2 ensemble mean and observation in the spatial distributions of dynamic and thermodynamic effects can be attributed to the suppressed natural variability. Several ensemble members of LENS2, however, capture the maximum thermodynamic effect in the Arctic as in GOGA2 and PAC2 (Fig.S8), further suggesting the considerable role of internal variability in the simulated Arctic AR increases.

Summary

In this study, we show a robust frequency increase in ARs that penetrate into the Arctic in the ice growing season in recent decades, especially over the ABK region. ARs, which dominate the

Arctic moisture import, induce a strong melting effect, especially on the newly-formed thin and fragile sea ice, through enhanced downward longwave radiation from the AR-transported water vapor and heat and the associated liquid rainfall. Given the thinner ice cover aggravated by warmer ocean water mass[e.g., 9,11–14], more frequent ARs result in a stronger melting effect on sea ice in the winter ice growing season, slowing down the seasonal sea ice recovery in recent decades and accounting for 34(±2)% of the observed sea ice area decline in early winter ABK. Using state-of-the-art model ensembles and a novel pacemaker approach, we further demonstrate that, in addition to a uniform AR increase in response to anthropogenic forcing, the observed tropical Pacific SST variability is indispensable in producing the observed AR changes around the Arctic in the past few decades. The increased frequency in Arctic ARs, in turn, is mainly due to the warming-driven moistening.

The AR frequency increase manifests the intensifying hydrological cycle in the Arctic[42–44], and could exert impacts beyond hydrology and the cryosphere in the Arctic. Combined with more frequent cyclones in the central Arctic and Chukchi Sea[45–47], the resultant rainfall and snowfall are expected to experience pronounced changes[48,49], leading to a more stormy Arctic. These changes will increase the ecosystem fragility and human exposure to natural hazards in the Arctic as international ocean freight and fishing industries are expected to grow there in the coming decades. Advancing our understanding of the changes in the synoptic weather systems such as ARs in a warming climate could lead to more credible projections of ecosystem changes and human adaptation to the growing impacts of global warming in the polar region.

Methods

Observational datasets

Three reanalysis datasets are employed in this study: the European Centre for Medium-Range Weather Forecasts (ECMWF) 5th generation reanalysis (ERA5)[50] in 1979-2021 at a resolution of 0.5°×0.5°, National Aeronautics and Space Administration (NASA) Modern-Era Retrospective analysis for Research and Applications, version 2 (MERRA2)[51] in 1980-2021 at 0.625°×0.5°, and Japan Meteorological Agency Japanese 55-year Reanalysis (JRA55)[52] in 1979-2021 at 1.5°×1.5°. We focus on the long-term changes in the sea ice seasonal recovery months November-December-January (NDJ), and thus there are 42 NDJ in ERA5 and JRA55, and 41 NDJ in MERRA2 analyzed. Daily variables are used, but the results are robust using 6-hourly data (See Fig.S1a vs Fig.2a). See Supplementary Information (SI) for the quality and validation of reanalysis data.

The sea ice data is NOAA/National Snow and Ice Data Center (NSIDC) climate data record of satellite passive microwave sea ice concentration (SIC), version 4[53]. Both daily and monthly SIC estimates during 1979-2021 from the NASA Bootstrap algorithm on a 25km×25km grid are used. Note that satellite observation is missing during the 1987-88 winter. The sea ice cover edge is defined as the 15% contour of SIC by convention. Sea ice coverage can be measured in terms of

both area and extent (see NSIDC terminology: https://nsidc.org/cryosphere/seaice/data/terminology.html). Sea ice extent (SIE) measures the ocean region surrounded by sea ice cover edge line. Sea ice area (SIA) at each grid cell is calculated as SIC multiplying the cell area, i.e., the area of the portion of the cell covered by ice. For example, for a grid cell with SIC of 50%, the whole grid cell is treated as ice covered (SIC>15%) in determining SIE, while only 50% of the grid cell is counted in SIA. There is almost no difference between SIE and SIA from the view of long-term change and large scale. We use SIA in this study because SIA represents the exact variations of sea ice coverage and thus is appropriate to reflect the ARs' impact at the synoptic temporal and spatial scales. The NDJ SIA growth in Fig.4 is defined as the cumulative sum of daily anomalies of SIA tendency in NDJ. The SIA tendency on the *i* day is defined as $(SIA_{i+1}-SIA_{i-1})/2$, where *i* denotes the day number during Nov.1-Jan.31. The daily anomaly is the deviation from the daily mean of the whole study period of each dataset smoothed with a 15-day moving average window. SIA growth associated with (without) AR is the cumulated sum of SIA tendency with (without) AR occurrence. We focus on ice coverage because of the distinct surface energy balance and air-sea interaction with and without ice cover on the sea surface.

Model experiments and interpretation

This study involves a series of model ensemble experiments conducted by Climate Variability and Change Working Group (CVCWG, https://www.cesm.ucar.edu/working_groups/CVC/) at National Center for Atmospheric Research (NCAR) using the state-of-the-art global climate model CESM2. First, the 50-member CESM2 Large Ensemble (LENS2)[54] outputs are employed. LENS2 covers the period 1850-2100 under CMIP6 historical (before 2014) and SSP370 (from 2015) future radiative forcing scenarios. Each ensemble member is forced in an identical way, except for the initial conditions. The LENS2 ensemble can be regarded as an expansion set of the CESM2 simulations in the CMIP6 archive. The results in LENS2 are therefore generally similar to the CESM2 simulations in CMIP6, which we have confirmed. Second, we examine a 10-member atmosphere-only simulation from CAM6, the atmospheric component of CESM2, forced by the same external forcing as LENS2 and prescribed time-varying SST from NOAA Extended Reconstruction Sea Surface Temperature Version 5 (ERSSTv5) and Hadley Centre sea ice (HadISST1) from 1880-2019, named as Global Ocean Global Atmosphere. This set of simulations is called GOGA2 to differentiate it from a similar set of simulations produced by CAM5/CESM1. Third, we analyze a 10-member pacemaker historical experiment with CESM2 in which the time-evolving SST anomalies (SSTa) in the tropical Pacific are nudged to observations (ERSSTv5). The nudging mask covers the tropical Pacific from the American coast to the western Pacific between 20°S-20°N, with the form of a wedge shape toward the Maritime Continent to the west of the dateline, and a 5-degree buffer region where the strength of the relaxation is linearly reduced. In each pacemaker run, the model simulated temporal SSTa is replaced with the observed evolution of SSTa (i.e., the tropical Pacific SSTa is the pacemaker), with the rest of the model's coupled climate system free to evolve. Since only the anomalies are nudged, the nudging does not alter the

mean state of the model. In the period of 1980s-2010s, there is a decadal cooling trend in the tropical Pacific (i.e., a La-Nina-like change), known as the phase transition of Inter-decadal Pacific Oscillation (IPO) or Pacific Decadal Oscillation (PDO), the leading mode of internal variability at the decadal timescale featuring SST variability in the Pacific Ocean. See the webpage (https://www.cesm.ucar.edu/working_groups/CVC/simulations/cesm2-pacific_pacemaker.html) for the nudging mask area and the details of the Pacific Pacemaker experiments. This CESM2 Pacific Pacemaker ensemble is called PAC2 in this study.

The daily and monthly outputs are available at the same resolution of 0.9°×1.25°. We only analyzed the outputs in 1979-2014 in which all experiments are forced by the historical forcing to facilitate a comparison to the observations, i.e., 35 NDJ in each member for analysis.

As the three experiments (GOGA2, LENS2, and PAC2) share the same radiative forcing and use the same atmospheric model, the differences among them lie in the surface boundary conditions for the atmosphere: prescribed observed SST (GOGA2), coupled ocean-atmosphere except for the tropical Pacific SST which is constrained by the observed IPO evolution (PAC2), and fully coupled ocean-atmosphere (LENS2). With these experimental setups, the climate evolution in GOGA2 is most comparable to observations, followed by PAC2, while LENS2 is free to evolve subject only to external forcing.

We interpret the model results following the well established approach in the climate modeling community[e.g., 55–57]. The observed climate reflects the combination of the radiatively forced response and a specific realization of the natural variability. Because the latter is random, we would not expect an individual member of the free running model ensembles to closely resemble the observation. Although free running models cannot perfectly reproduce the exact phase of the observed natural variability, model ensembles can be used to separate the influences of external forcing and internal variability. The influence of anthropogenic forcing, i.e., the forced response, can be estimated by the ensemble mean of LENS2, because each member of the ensemble is influenced by the same external forcing while the internal variability is largely suppressed by averaging across the individual ensemble members which feature different realizations of the random natural variability. In other words, the spread among the ensemble members in LENS2 represents the effects of random internal variability. With the tropical Pacific SSTa nudged to the observations, the PAC2 ensemble spread represents internal variability associated with regions outside the tropical Pacific and with internal atmospheric dynamics, while its ensemble mean reflects the combination of the anthropogenically forced responses and the model's responses to the observed tropical Pacific SST variability. Since PAC2 and LENS2 share the same model configurations, their forced responses should in principle be the same, and therefore the forced response in both LENS2 and PAC2 can be represented by the ensemble mean of LENS2. Then, the role of the tropical Pacific SST variability, called "tropical Pacific influence", can be isolated by subtracting the LENS2 ensemble mean from the PAC2 mean[55–57]. The tropical Pacific influence

is an estimate of the variability in the climate system that is associated with tropical Pacific SSTs. Ref[55] concluded that this approach allows us to consistently compare the magnitude of climate responses (for example, Arctic AR changes) to anthropogenic forcing and tropical Pacific variability. The significant difference between the PAC2 and LENS2 mean AR trends in northern ABK and inland Eurasia (Fig.5d) suggests that the Pacific variability played a detectable role in the high-latitude AR trend during recent decades.

There are caveats in understanding the influence of tropical Pacific variability based on the model experiments. First, the estimate of the tropical influence assumes that the responses to tropical Pacific variability and external forcings are independent. Indeed, they are largely linearly separable for all practical purposes[e.g., 58–60], although this assumption may not strictly hold. In any case, it is difficult to completely separate the external and tropical signals. Thus, the linear assumption in fact neglects the impact of external forcing on tropical Pacific variability[55]. Second, it is possible that the forced response in LENS2 and PAC2 may not be the same. Nevertheless, many previous studies have shown that the above approach practically and realistically delineates the response to tropical Pacific variability[e.g., 55–57].

Third, some biases in model physics may affect sea ice simulation and ARs' impact on sea ice in CESM2. Over the Arctic, the CESM2 configuration has thinner liquid clouds and less cloud fraction due to underestimated aerosols, leading to much more shortwave radiation received by sea ice in melt season and thus an insufficient late summer Arctic sea ice cover, while the sea ice coverage bias is relatively small in winter[e.g., 61,62]. The sea ice bias could produce a faster ice growth in early winter, debasing the significance of ARs' melting effect on sea ice in CESM2 simulations, as we can see in Fig.4. In addition, less cloud fraction may also reduce the contribution of cloud to DLW. On the other hand, the winter ice thickness in CESM2 is biased thin in historical simulations[63], which could enhance the ARs' melting effect. That is to say, biases in CESM2 physics may partly cancel each other to simulate the ARs' impact on sea ice, and could explain the weaker melting effect of ARs simulated in PAC2 than observation (Fig.4). Furthermore, given that the Gulf stream warming in CESM2 lies towards the higher end of CMIP6 models[64], the underestimation of the winter SIC decline in Barents-Kara Seas in recent decades in CESM2 (See[64] or Fig.S4) may be attributable to the underestimation of atmospheric influences such as the weaker ARs' melting effect in CESM2. Nevertheless, given that the ensembles employed in the current study are based on the same model, the model bias may be canceled when one ensemble is subtracted from another and thus may not affect the understanding of the tropical Pacific influence obtained from (PAC2 minus LENS2).

AR detection and analysis methods

We employ an IVT-based AR detection algorithm originally developed by ref[65] and slightly optimize it for the Arctic following ref[24]. The algorithm by ref[65] is recommended by the Atmospheric River Tracking Method Intercomparison Project (ARTMIP), especially for research

on ARs in polar latitudes and inland regions[66]. ARTMIP noted that this algorithm is one of the methods that facilitate the attribution of impacts within the AR footprint[66]. In fact, all ARTMIP global algorithms tend to agree remarkably well on the AR footprints[67]. In the algorithm used in this study, the monthly dependent 85th percentile of the IVT magnitude at each grid cell, or 100 kg m^{-1} s^{-1}, whichever is greater, is used as the intensity threshold to identify contiguous regions with elevated IVT. In practice, the 85th percentile IVT is the threshold used in the midlatitudes, same as many other algorithms[66], while 100 kg m^{-1} s^{-1} is the actual threshold used in the Arctic region because of the low IVT due to low air temperature. We also checked the ARs with relative thresholds in the Arctic and the results are not sensitive to the choice of thresholds (See the discussion in SI and FigS.1 d-f). Potential ARs are then filtered by applying size, length, length-to-width ratio, coherence, the meridional component of mean IVT, and mean transport direction criteria. We follow ref[24] to change the length criterion from 2000km to 1500km, considering the ARs reaching the Arctic are usually at the end of their lifecycle and their size shrinks (In fact, the results are not sensitive to the change of length criterion, not shown). These requirements ensure that the identified characteristics are long, narrow, coherent belts of poleward moisture transport in (and connecting) the midlatitudes and polar regions, i.e., they bear the features of ARs. See refs[24,65] for additional details on the AR detection algorithm.

A scaling method[33] is employed to separate the thermodynamic effect and the dynamical effect in the AR frequency trend. We create a hypothetical scenario of daily IVT with dynamic effect only by applying a scaling coefficient to specific humidity, given the moisture changes are expected to scale in line with the CC relationship. Specifically, the specific humidity is scaled by a factor, q_c/q_y, where q_c is the climatological specific humidity in NDJ at the level and grid to which this factor applies and q_y is the mean specific humidity at the same grid for the given NDJ. By scaling the data this way, the year-to-year change in specific humidity is removed. Then, the IVT calculated with the scaled moisture field and the same threshold are used as input to the AR detection algorithm. As a result, the effect of the background moisture interannual variability on AR variability is suppressed, allowing the AR trend due to the dynamic effect to be estimated. Ref[68] found that the two components are largely linearly additive using the same method. Therefore, we calculate the thermodynamic effect as the difference between the total trend and the dynamic effect.

Variable (DLW, rainfall, snowfall, SIC, etc.) anomalies associated with ARs at a grid are detected if an AR appears at this grid. The climatology or reference state refers to the mean of the whole study period of each dataset smoothed with a 15-day moving average window. For the AR-related trends in variables (DLW, cloud radiative effect, rainfall, and snowfall) shown in Fig.3, Fig.S2b, Fig.S5, and Fig.S6, we first integrate the variable associated with ARs in NDJ over time (i.e., the total/cumulated amount of these fluxes related to ARs) and then calculate the trends. The contribution of cloud radiative effect to DLW is the difference between surface DLW and clear sky DLW. The results are qualitatively similar if we take into account the persistence (3-day after

landfall even the ARs decay, Fig.1c) of ARs' impact in detecting the AR-related variable anomalies (not shown). The impact of ice drifting related to AR wind on ABK SIA is much smaller than that of AR's melting effect (see SI) and thus not be involved in this study.

Linear projection is used to determine the amount of enhancement of AR melting effect due to AR frequency increase. We first calculate the melting effect on SIA corresponding to 1% AR frequency (~0.92 day) occurrence based on the SIA growth with AR (red line in Fig.4) and AR frequency (Fig.2b) in NDJ, which on average is a reduction of -8.8(±0.6)×10^4 km^2 in ABK SIA in NDJ in the observation. Uncertainty is measured by the standard error computed from interannual time series. Then we can estimate the enhancement of the melting effect due to AR frequency increase by projecting the SIA reduction corresponding to 1% AR frequency to the actually trend in AR frequency (Fig.2b), and finally infer its contribution (~34% ±2%) to the SIA decline in ABK in NDJ (red line in Fig.2b). The contribution is 30(±5)% in PAC2 due to a weaker melting effect simulated in CESM2. The uncertainty in PAC2 is the standard error cross ensemble members.

Statistics methods

The Student *t*-test is used in the significance test for the linear trend in observations. A 1000-trail bootstrap resampling with replacement is used in the significance tests for the composite analysis and the trends in model ensembles. Following Ref[69], the uncertainty in the mean trend of an ensemble is represented by the 95% confidence interval, which is given by $\overline{b} \pm \frac{cs_b}{\sqrt{n}}$, where $\overline{b}$ is the ensemble mean of the trends calculated from individual ensemble members, *n* is the ensemble size, *c* is the 97.5th percentile of the Student's *t* distribution with *n*-1 degrees of freedom, s_b is an estimate of the inter-member variance of the trends. We calculate this 95% confidence interval for GOGA2, LENS2, and PAC2, shown as the vertical color bars in Fig.5e. The pattern correlation coefficient (PCC) is employed to measure the pattern similarity between the individual run of LENS2 and the ensemble mean of GOGA2 (PAC2) with latitudinal weights considered.

Data availability

The data acquisition information for the simulations used in this study can be found on CVCWG/NCAR webpage (https://www.cesm.ucar.edu/working_groups/CVC/). ERA5, MERRA2, and JRA55 reanalysis data are available from https://cds.climate.copernicus.eu/#!/home, https://gmao.gsfc.nasa.gov/reanalysis/MERRA-2/data_access/, and https://jra.kishou.go.jp/JRA-55/index_en.html. NSIDC sea ice concentration is available from https://nsidc.org/data/G02202. See SI for the download information of the data used in SI.

Code availability

The code of the AR detection method used in this study can be downloaded at: https://doi.org/10.25346/S6/SJGRKY. Other analysis codes are available from the corresponding author upon request.

480 **References**

481 1. Stroeve, J. C. *et al.* Trends in Arctic sea ice extent from CMIP5, CMIP3 and observations.
482 *Geophys. Res. Lett.* **39**, L16502 (2012).
483 2. Bailey, H. *et al.* Arctic sea-ice loss fuels extreme European snowfall. *Nature Geoscience* 1–6
484 (2021) doi:10.1038/s41561-021-00719-y.
485 3. Cohen, J., Agel, L., Barlow, M., Garfinkel, C. I. & White, I. Linking Arctic variability and
486 change with extreme winter weather in the United States. *Science* (2021)
487 doi:10.1126/science.abi9167.
488 4. Dalpadado, P. *et al.* Productivity in the Barents Sea - Response to Recent Climate
489 Variability. *PLOS ONE* **9**, e95273 (2014).
490 5. Fossheim, M. *et al.* Recent warming leads to a rapid borealization of fish communities in the
491 Arctic. *Nature Clim Change* **5**, 673–677 (2015).
492 6. Park, D.-S. R., Lee, S. & Feldstein, S. B. Attribution of the Recent Winter Sea Ice Decline
493 over the Atlantic Sector of the Arctic Ocean. *J. Clim.* **28**, 4027–4033 (2015).
494 7. Woods, C. & Caballero, R. The Role of Moist Intrusions in Winter Arctic Warming and Sea
495 Ice Decline. *Journal of Climate* **29**, 4473–4485 (2016).
496 8. Hofsteenge, M. G., Graversen, R. G., Rydsaa, J. H. & Rey, Z. The impact of atmospheric
497 Rossby waves and cyclones on the Arctic sea ice variability. *Clim Dyn* (2022)
498 doi:10.1007/s00382-022-06145-z.
499 9. Petty, A. A., Holland, M. M., Bailey, D. A. & Kurtz, N. T. Warm Arctic, Increased Winter
500 Sea Ice Growth? *Geophysical Research Letters* **45**, 12,922-12,930 (2018).
501 10. Stroeve, J. & Notz, D. Changing state of Arctic sea ice across all seasons. *Environ. Res. Lett.*
502 **13**, 103001 (2018).
503 11. Barton, B. I., Lenn, Y.-D. & Lique, C. Observed Atlantification of the Barents Sea Causes
504 the Polar Front to Limit the Expansion of Winter Sea Ice. *Journal of Physical Oceanography*
505 **48**, 1849–1866 (2018).
506 12. Polyakov, I. V. *et al.* Borealization of the Arctic Ocean in Response to Anomalous
507 Advection From Sub-Arctic Seas. *Frontiers in Marine Science* **7**, (2020).
508 13. Skagseth, Ø. *et al.* Reduced efficiency of the Barents Sea cooling machine. *Nature Climate*
509 *Change* **10**, 661–666 (2020).
510 14. Tsubouchi, T. *et al.* Increased ocean heat transport into the Nordic Seas and Arctic Ocean
511 over the period 1993–2016. *Nat. Clim. Chang.* **11**, 21–26 (2021).
512 15. Nash, D., Waliser, D., Guan, B., Ye, H. & Ralph, F. M. The Role of Atmospheric Rivers in
513 Extratropical and Polar Hydroclimate. *Journal of Geophysical Research: Atmospheres* **123**,
514 6804–6821 (2018).
515 16. Ralph, F. M. *et al.* Atmospheric Rivers Emerge as a Global Science and Applications Focus.
516 *Bulletin of the American Meteorological Society* **98**, 1969–1973 (2017).
517 17. Zhu, Y. & Newell, R. E. A Proposed Algorithm for Moisture Fluxes from Atmospheric
518 Rivers. *Monthly Weather Review* **126**, 725–735 (1998).

18. Newman, M., Kiladis, G. N., Weickmann, K. M., Ralph, F. M. & Sardeshmukh, P. D. Relative Contributions of Synoptic and Low-Frequency Eddies to Time-Mean Atmospheric Moisture Transport, Including the Role of Atmospheric Rivers. *J. Climate* **25**, 7341–7361 (2012).
19. Lavers, D. A. & Villarini, G. The contribution of atmospheric rivers to precipitation in Europe and the United States. *Journal of Hydrology* **522**, 382–390 (2015).
20. Chen, X., Leung, L. R., Wigmosta, M. & Richmond, M. Impact of Atmospheric Rivers on Surface Hydrological Processes in Western U.S. Watersheds. *Journal of Geophysical Research: Atmospheres* **124**, 8896–8916 (2019).
21. Skinner, C. B., Lora, J. M., Payne, A. E. & Poulsen, C. J. Atmospheric river changes shaped mid-latitude hydroclimate since the mid-Holocene. *Earth and Planetary Science Letters* **541**, 116293 (2020).
22. Hegyi, B. M. & Taylor, P. C. The Unprecedented 2016–2017 Arctic Sea Ice Growth Season: The Crucial Role of Atmospheric Rivers and Longwave Fluxes. *Geophysical Research Letters* **45**, 5204–5212 (2018).
23. Gorodetskaya, I. V. *et al.* The role of atmospheric rivers in anomalous snow accumulation in East Antarctica. *Geophysical Research Letters* **41**, 6199–6206 (2014).
24. Mattingly, K. S., Mote, T. L. & Fettweis, X. Atmospheric River Impacts on Greenland Ice Sheet Surface Mass Balance. *Journal of Geophysical Research: Atmospheres* **123**, 8538–8560 (2018).
25. Wille, J. D. *et al.* West Antarctic surface melt triggered by atmospheric rivers. *Nature Geoscience* **12**, 911–916 (2019).
26. Francis, D., Mattingly, K. S., Temimi, M., Massom, R. & Heil, P. On the crucial role of atmospheric rivers in the two major Weddell Polynya events in 1973 and 2017 in Antarctica. *Science Advances* **6**, eabc2695 (2020).
27. Persson, P. O. G., Shupe, M. D., Perovich, D. & Solomon, A. Linking atmospheric synoptic transport, cloud phase, surface energy fluxes, and sea-ice growth: observations of midwinter SHEBA conditions. *Clim Dyn* **49**, 1341–1364 (2017).
28. Doyle, S. H. *et al.* Amplified melt and flow of the Greenland ice sheet driven by late-summer cyclonic rainfall. *Nature Geosci* **8**, 647–653 (2015).
29. Ledley, T. S. Snow on sea ice: Competing effects in shaping climate. *Journal of Geophysical Research: Atmospheres* **96**, 17195–17208 (1991).
30. Merkouriadi, I., Cheng, B., Hudson, S. R. & Granskog, M. A. Effect of frequent winter warming events (storms) and snow on sea-ice growth – a case from the Atlantic sector of the Arctic Ocean during the N-ICE2015 campaign. *Annals of Glaciology* **61**, 164–170 (2020).
31. Wang, Z., Walsh, J., Szymborski, S. & Peng, M. Rapid Arctic Sea Ice Loss on the Synoptic Time Scale and Related Atmospheric Circulation Anomalies. *Journal of Climate* **33**, 1597–1617 (2020).

32. Gao, Y., Lu, J. & Leung, L. R. Uncertainties in Projecting Future Changes in Atmospheric Rivers and Their Impacts on Heavy Precipitation over Europe. *J. Clim.* **29**, 6711–6726 (2016).
33. Ma, W., Chen, G. & Guan, B. Poleward Shift of Atmospheric Rivers in the Southern Hemisphere in Recent Decades. *Geophysical Research Letters* **47**, e2020GL089934 (2020).
34. Payne, A. E. *et al.* Responses and impacts of atmospheric rivers to climate change. *Nature Reviews Earth & Environment* **1**, 143–157 (2020).
35. Yang, W. & Magnusdottir, G. Springtime extreme moisture transport into the Arctic and its impact on sea ice concentration. *Journal of Geophysical Research: Atmospheres* **122**, 5316–5329 (2017).
36. Onarheim, I. H. & Årthun, M. Toward an ice-free Barents Sea. *Geophysical Research Letters* **44**, 8387–8395 (2017).
37. Meehl, G. A., Chung, C. T. Y., Arblaster, J. M., Holland, M. M. & Bitz, C. M. Tropical Decadal Variability and the Rate of Arctic Sea Ice Decrease. *Geophysical Research Letters* **45**, 11,326-11,333 (2018).
38. Wu, Y., Lu, J., Ding, Q. & Liu, F. Linear Response Function Reveals the Most Effective Remote Forcing in Causing September Arctic Sea Ice Melting in CESM. *Geophysical Research Letters* **48**, e2021GL094189 (2021).
39. Gettelman, A. *et al.* High Climate Sensitivity in the Community Earth System Model Version 2 (CESM2). *Geophysical Research Letters* **46**, 8329–8337 (2019).
40. Luo, D. *et al.* Impact of Ural Blocking on Winter Warm Arctic–Cold Eurasian Anomalies. Part I: Blocking-Induced Amplification. *Journal of Climate* **29**, 3925–3947 (2016).
41. Clark, J. P. & Lee, S. The Role of the Tropically Excited Arctic Warming Mechanism on the Warm Arctic Cold Continent Surface Air Temperature Trend Pattern. *Geophys. Res. Lett.* **0**, (2019).
42. Vihma, T. *et al.* The atmospheric role in the Arctic water cycle: A review on processes, past and future changes, and their impacts. *Journal of Geophysical Research: Biogeosciences* **121**, 586–620 (2016).
43. Gimeno, L. *et al.* Atmospheric moisture transport and the decline in Arctic Sea ice. *WIREs Climate Change* **10**, e588 (2019).
44. Bintanja, R. *et al.* Strong future increases in Arctic precipitation variability linked to poleward moisture transport. *Science Advances* **6**, eaax6869 (2020).
45. Zhang, X., Walsh, J. E., Zhang, J., Bhatt, U. S. & Ikeda, M. Climatology and Interannual Variability of Arctic Cyclone Activity: 1948–2002. *Journal of Climate* **17**, 2300–2317 (2004).
46. Zahn, M., Akperov, M., Rinke, A., Feser, F. & Mokhov, I. I. Trends of Cyclone Characteristics in the Arctic and Their Patterns From Different Reanalysis Data. *Journal of Geophysical Research: Atmospheres* **123**, 2737–2751 (2018).

47. Valkonen, E., Cassano, J. & Cassano, E. Arctic Cyclones and Their Interactions With the Declining Sea Ice: A Recent Climatology. *Journal of Geophysical Research: Atmospheres* **126**, e2020JD034366 (2021).
48. Webster, M. A., Parker, C., Boisvert, L. & Kwok, R. The role of cyclone activity in snow accumulation on Arctic sea ice. *Nat Commun* **10**, 5285 (2019).
49. McCrystall, M. R., Stroeve, J., Serreze, M., Forbes, B. C. & Screen, J. A. New climate models reveal faster and larger increases in Arctic precipitation than previously projected. *Nat Commun* **12**, 6765 (2021).
50. Hersbach, H. *et al.* The ERA5 global reanalysis. *Quarterly Journal of the Royal Meteorological Society* **146**, 1999–2049 (2020).
51. Gelaro, R. *et al.* The Modern-Era Retrospective Analysis for Research and Applications, Version 2 (MERRA-2). *Journal of Climate* **30**, 5419–5454 (2017).
52. Kobayashi, S. *et al.* The JRA-55 Reanalysis: General Specifications and Basic Characteristics. *Journal of the Meteorological Society of Japan. Ser. II* **93**, 5–48 (2015).
53. Meier, W. N., Fetterer, F., Windnagel, A. K. & Stewart, J. S. *NOAA/NSIDC Climate Data Record of Passive Microwave Sea Ice Concentration, Version 4*. https://doi.org/10.7265/efmz-2t65 (2021).
54. Rodgers, K. B. *et al.* Ubiquity of human-induced changes in climate variability. *Earth System Dynamics Discussions* 1–22 (2021) doi:10.5194/esd-2021-50.
55. Holland, P. R., Bracegirdle, T. J., Dutrieux, P., Jenkins, A. & Steig, E. J. West Antarctic ice loss influenced by internal climate variability and anthropogenic forcing. *Nat. Geosci.* **12**, 718–724 (2019).
56. Schneider, D. P. & Deser, C. Tropically driven and externally forced patterns of Antarctic sea ice change: reconciling observed and modeled trends. *Clim Dyn* **50**, 4599–4618 (2018).
57. Yang, D. *et al.* Role of Tropical Variability in Driving Decadal Shifts in the Southern Hemisphere Summertime Eddy-Driven Jet. *Journal of Climate* **33**, 5445–5463 (2020).
58. Ting, M., Kushnir, Y., Seager, R. & Li, C. Forced and Internal Twentieth-Century SST Trends in the North Atlantic*. *J. Clim.* **22**, 1469–1481 (2009).
59. DelSole, T., Tippett, M. K. & Shukla, J. A Significant Component of Unforced Multidecadal Variability in the Recent Acceleration of Global Warming. *Journal of Climate* **24**, 909–926 (2011).
60. Lu, J., Hu, A. & Zeng, Z. On the possible interaction between internal climate variability and forced climate change. *Geophysical Research Letters* **41**, 2962–2970 (2014).
61. DuVivier, A. K. *et al.* Arctic and Antarctic Sea Ice Mean State in the Community Earth System Model Version 2 and the Influence of Atmospheric Chemistry. *Journal of Geophysical Research: Oceans* **125**, e2019JC015934 (2020).
62. Kay, J. E. *et al.* Less Surface Sea Ice Melt in the CESM2 Improves Arctic Sea Ice Simulation With Minimal Non-Polar Climate Impacts. *Journal of Advances in Modeling Earth Systems* **14**, e2021MS002679 (2022).

63. DeRepentigny, P., Jahn, A., Holland, M. M. & Smith, A. Arctic Sea Ice in Two Configurations of the CESM2 During the 20th and 21st Centuries. *Journal of Geophysical Research: Oceans* **125**, e2020JC016133 (2020).
64. Yamagami, Y., Watanabe, M., Mori, M. & Ono, J. Barents-Kara sea-ice decline attributed to surface warming in the Gulf Stream. *Nat Commun* **13**, 3767 (2022).
65. Guan, B. & Waliser, D. E. Detection of atmospheric rivers: Evaluation and application of an algorithm for global studies. *J. Geophys. Res.* **120**, 12514–12535 (2015).
66. Rutz, J. J. *et al.* The Atmospheric River Tracking Method Intercomparison Project (ARTMIP): Quantifying Uncertainties in Atmospheric River Climatology. *Journal of Geophysical Research: Atmospheres* **124**, 13777–13802 (2019).
67. Lora, J. M., Shields, C. A. & Rutz, J. J. Consensus and Disagreement in Atmospheric River Detection: ARTMIP Global Catalogues. *Geophysical Research Letters* **47**, e2020GL089302 (2020).
68. Zhang, P., Chen, G., Ma, W., Ming, Y. & Wu, Z. Robust Atmospheric River Response to Global Warming in Idealized and Comprehensive Climate Models. *Journal of Climate* **34**, 7717–7734 (2021).
69. Swart, N. C., Fyfe, J. C., Gillett, N. & Marshall, G. J. Comparing Trends in the Southern Annular Mode and Surface Westerly Jet. *Journal of Climate* **28**, 8840–8859 (2015).

Acknowledgments

We thank Jian Lu at PNNL, Sukyoung Lee and Steven B. Feldstein at PSU for helpful discussion. We would like to acknowledge the CVCWG/NCAR for conducting the CESM2 simulations used in this study and thank Adam Philips and Isla Simpson at NCAR for helpful information on these model outputs. G.C. was supported by NSF Grants AGS-1832842 and NASA Grant 80NSSC21K1522. M.T. was funded by NASA award 80NSSC20K1254 and NSF award OPP-1825858. L.R.L was supported by the Office of Science, U.S. Department of Energy Biological and Environmental Research as part of the Regional and Global Model Analysis program area. B.G. was supported by NASA and the California Department of Water Resources.

Author contributions

P.Z. conceived the study, analyzed the data, and wrote the initial draft of the manuscript. G.C., M.T., and L.R.L. provided feedback on analysis and contributed to constructive revision. All authors contributed to editing and revision.

Competing interests

The authors declare no competing interests.

Figure list:

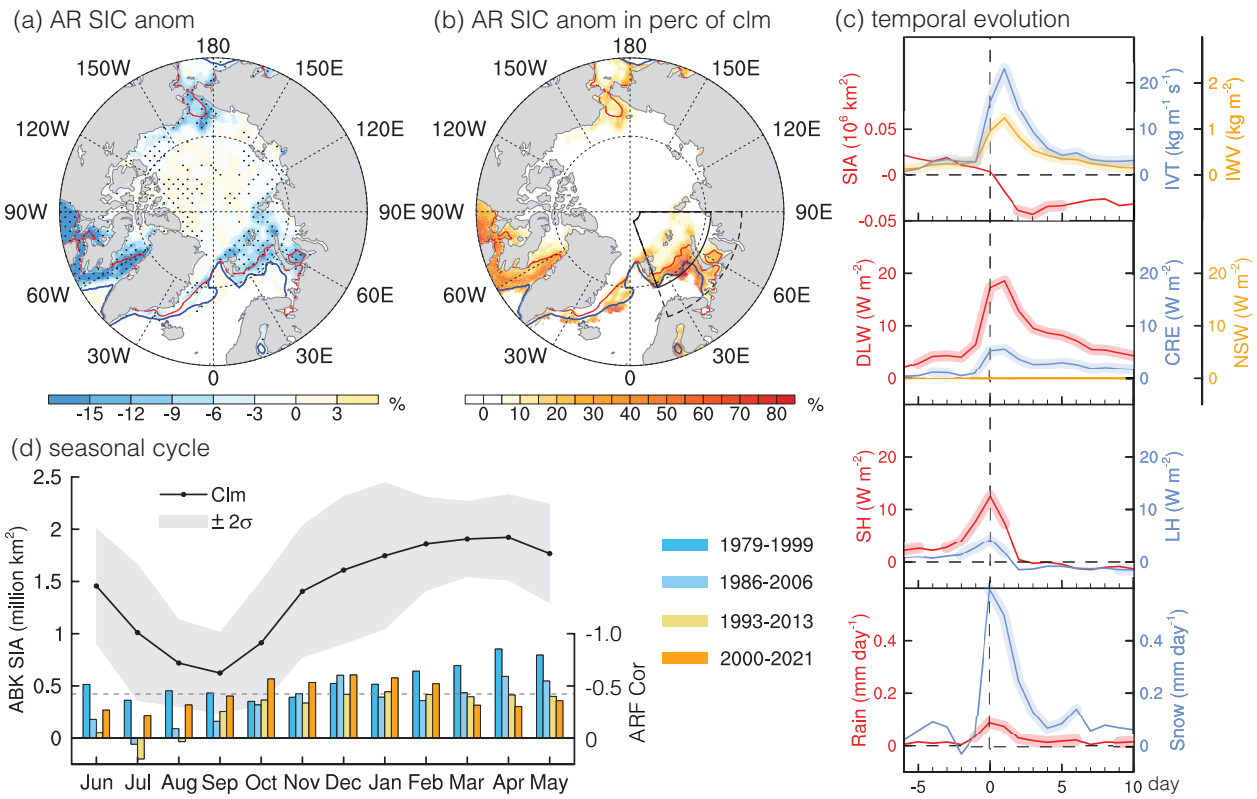

Fig. 1 **Relationship between ARs and Arctic sea ice.** (a) NSIDC sea ice concentration (SIC, units: %) anomalies associated with ARs in November-December-January (NDJ) in 1979-2021 (Methods). Red and blue lines are the climatological ice edges on Oct.31 and Jan.31, respectively, denoting the mean sea ice growth during NDJ. The region between these two ice edges is referred to as the marginal ice zone. (b) is the same as (a) but for the SIC anomalies in the percentage of climatology. The box (74°-88°*N*, 20°-90°*E*) highlights the Arctic-Barents-Kara (ABK) region. (c) Composite temporal evolution of the anomalies of the selected variables in ABK when ARs make "landfall" on the ice edge, including sea ice area (SIA), vertical integral of horizontal water vapor transport (IVT), vertical integral of water vapor (IWV), surface downward longwave radiation (DLW), cloud radiative effect (CRE) (the contribution of cloud to DLW), net surface shortwave radiation (NSW; almost zero), surface sensible heat flux (SH), surface latent heat flux (LH), rainfall, and snowfall. SIA is the total ice area in ABK calculated based on NSIDC SIC (Method), while other variables are area-averaged from ERA5 reanalysis data. Day-0 is the day of AR "landfalling" the ice cover (defined as at least one grid cell of an AR reaching the ice edge in ABK). The thick segments denote the anomalies are significant at the 95% confidence level. (d) Seasonal cycle of SIA over the ABK region and its correlation with AR frequency. Given the ice cover around ABK in winter may extend to the coast, we extend the southern boundary of the ABK area to 68°*N* (the dashed line in b) for the SIA calculation. Black line is the climatology in 1979-2021 with an interval of 2 standard deviations (gray shading). The bars are the correlation coefficients between AR frequency and SIA in four overlapping 21-year segments (see legend) in 1979-2021. The associated y-axis is on the right and inverted. Three-month running average is

applied before the correlation calculation, i.e., the bars in Dec indicate the values of NDJ. The bars exceeding the dashed line denote the correlation is significant at the 95% confidence level.

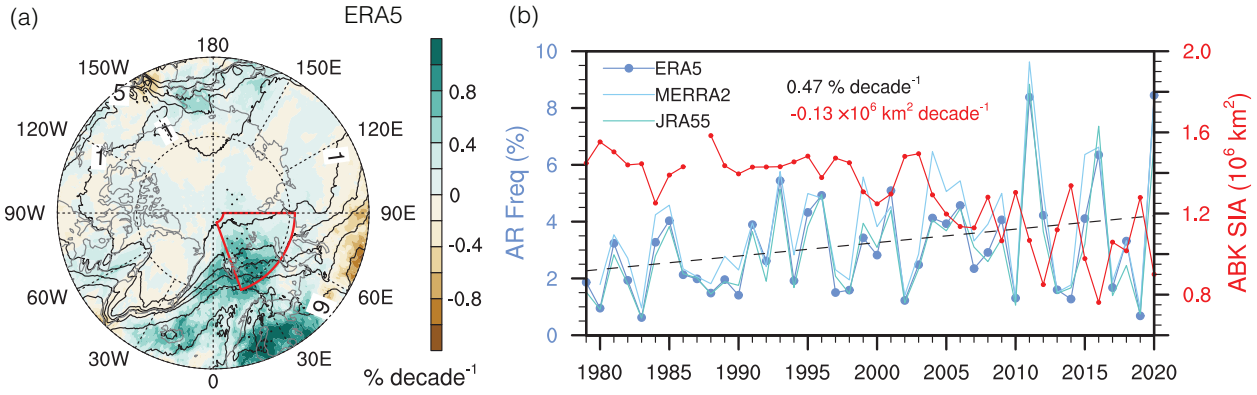

Fig. 2 **Arctic AR frequency trends in recent decades**. (a) AR frequency trends (color shading) in NDJ in 1979-2021 from the ERA5 reanalysis. Contours are the climatology. (b) Area-averaged AR frequency time series in the ABK area (highlighted by the box in a) from three reanalysis datasets (ERA5, MERRA2, and JRA55). The dashed gray line is the linear trend of the ensemble mean of the three datasets. The red line is the time series of area sum SIA in ABK with missing data in the NDJ of 1987-88. Both the AR and SIA trends are significant at the 95% confidence level using *t*-test.

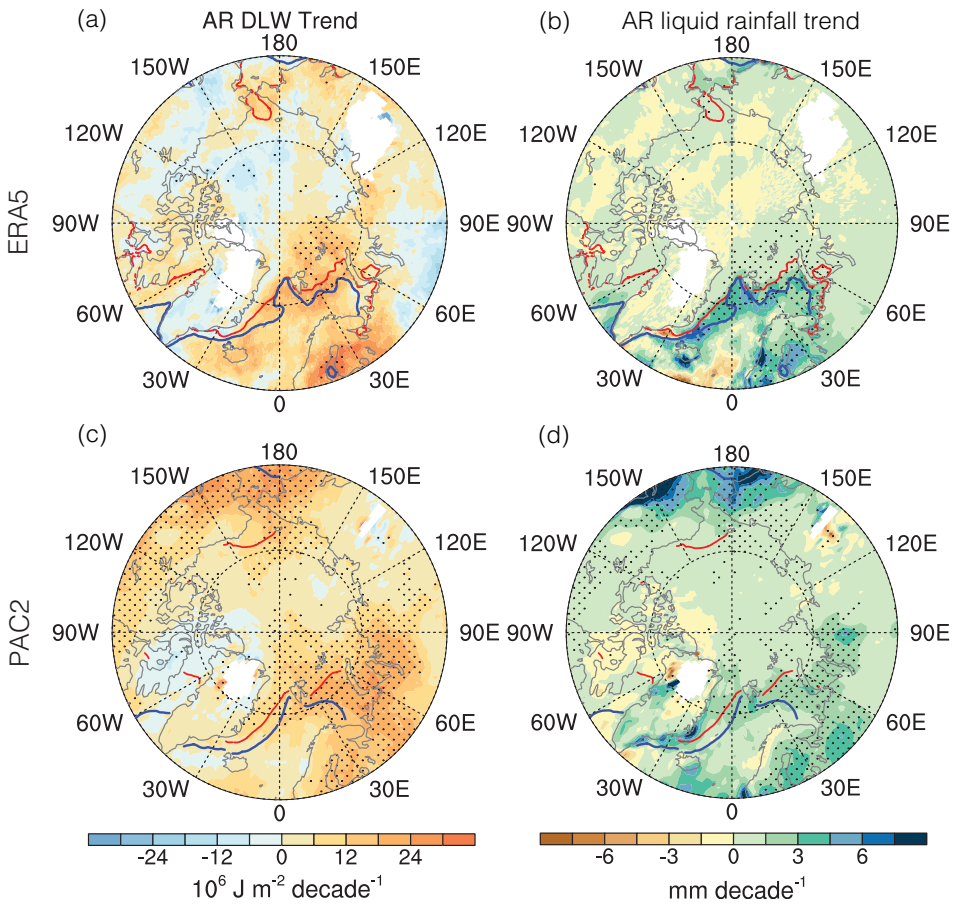

Fig. 3 **Trends in the physical processes related to AR melting effect in recent decades.** Linear trends in cumulated DLW (a) and liquid rainfall (b) associated with ARs in NDJ in ERA5. See the calculation in Method. The AR-induced total DLW in ERA5 can be validated by the satellite observation CERES-SYN after 2000 (see Fig.S2). (c-d) the same as (a-b) but for the model ensemble from PAC2. Dots denote trends that are statistically significant at the 95% confidence level according to the *t*-test for ERA5 and the 1000-trail bootstrap resampling method for PAC2. Red and blue lines in (a-f) are the climatological sea ice cover edges on Oct.31 and Jan.31, respectively, denoting the mean sea ice growth in NDJ.

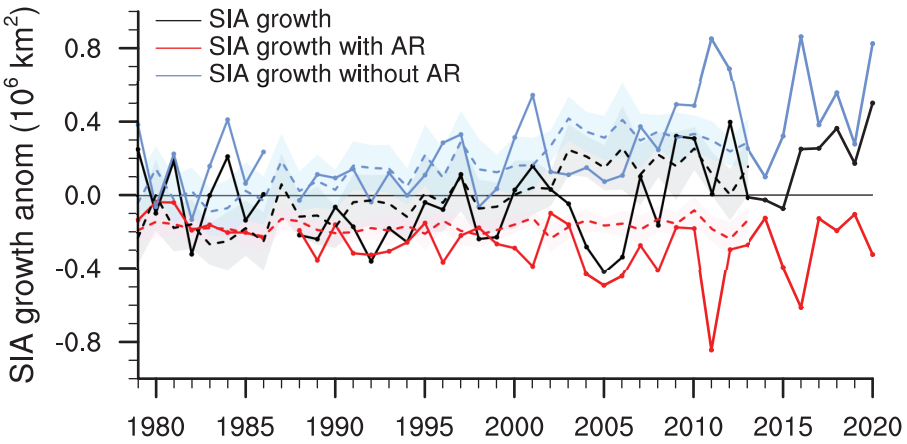

Fig. 4 **Sea ice area growth in early winter**. SIA growth is the cumulative sum of the daily anomalies of SIA day-to-day tendency in NDJ (Method). The solid lines denote the total SIA growth in the whole season (black), SIA growth associated with the ARs (red), SIA growth without the effects of ARs (light blue) in observation. The SIA growth associated with ARs denotes the melting effect of ARs on ABK SIA in NDJ. The negative trends of melting effect (red) and the positive trend in SIA growth without the impact of ARs (light blue) are significant at $P<0.01$, while the trend in whole season SIA growth (black) is less significant. The dashed lines show the SIA growth in PAC2 with standard error (color shading). The trend in melting effect in PAC2 is less significant, although PAC2 well reproduces the observed AR frequency change (see Fig.5). This may be attributable to the model bias in CESM2 sea ice simulations (see Method).

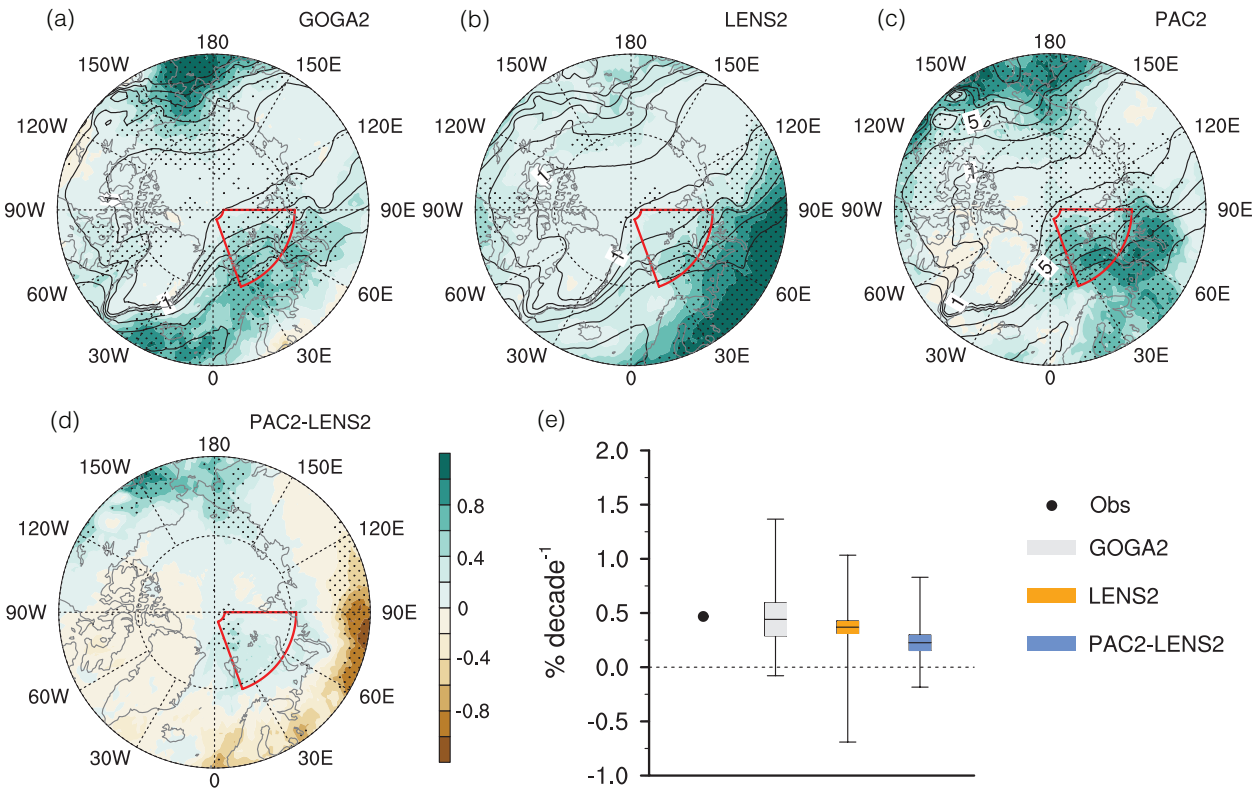

Fig. 5 **AR frequency trends in NDJ in model ensembles.** (a-c) Same as Fig.2(a) but for the GOGA2, LENS2, PAC2 ensembles. Agreements for the sign of AR changes among members of each ensemble are shown in Fig.S7. (d) AR changes due to tropical Pacific variability calculated as the difference between the ensemble means of PAC2 and LENS2 (see Model experiments and interpretation in Method). Dots denote trends that are statistically significant at 95% confidence level according to 1000-trail bootstrap resampling method in (a-d). (e) Uncertainties of area-averaged AR trends in each model ensemble. The horizontal lines inside the color bars represent the ensemble mean. The color bars show the 95% confidence interval (Method). The upper and lower whiskers denote the 5th and 95th percentiles of the trends across the ensemble (i.e., the minimum and maximum for GOGA2 and PAC2, 3rd minimum and maximum for LENS2). The blue bar is calculated based on the 10 members in PAC2 by removing the ensemble mean of LENS2, denoting the uncertainty of the contribution of tropical Pacific variability. The black dot shows the mean of the three reanalysis datasets, representing the observation. The LENS2 trend has a narrower confidence interval due to its larger ensemble size.

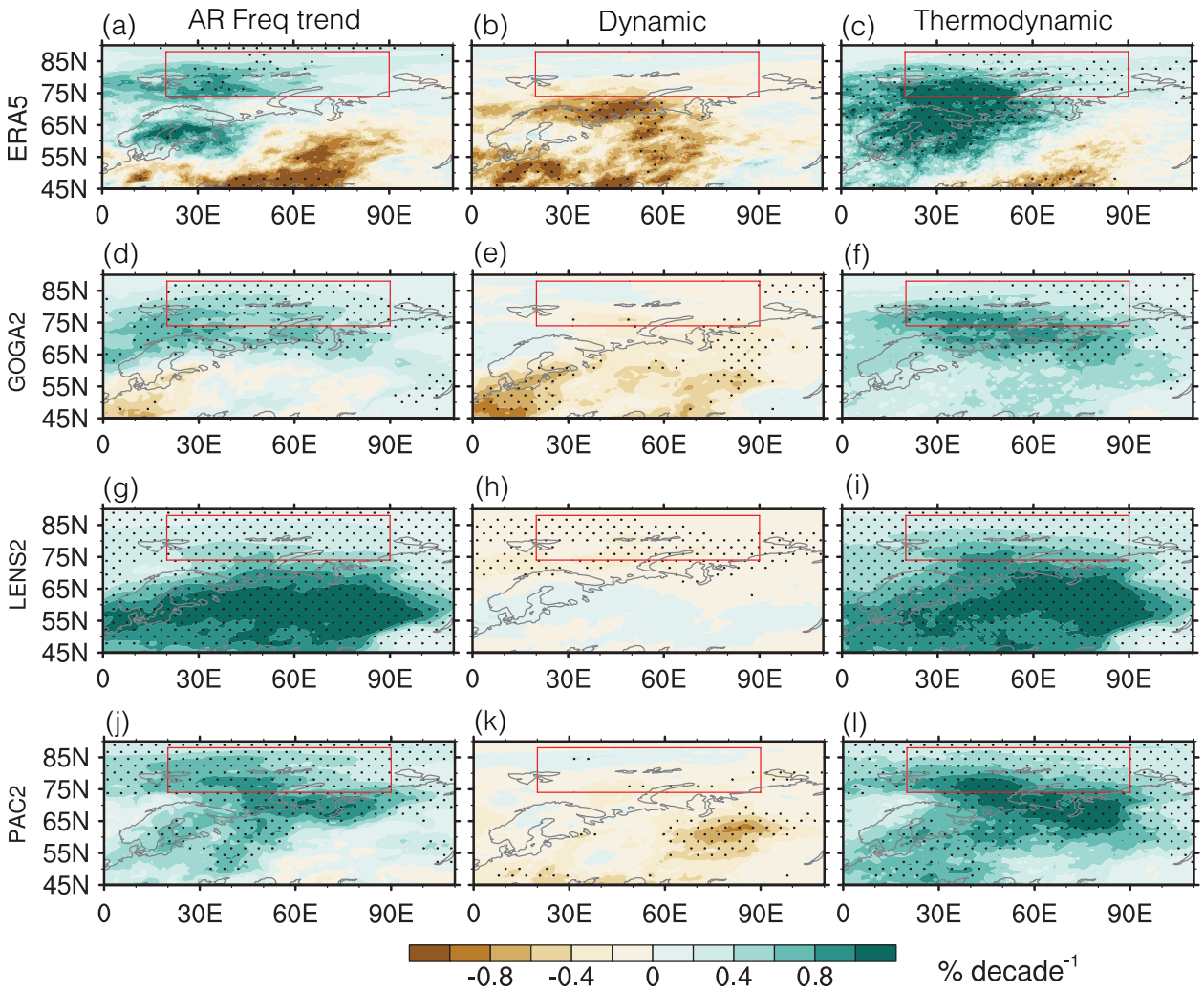

Fig. 6 **Mechanisms of the AR changes**. NDJ AR frequency trend in ERA5 (a), which is reproduced from Fig.2(a) but shown in cylindrical map projection here. Contributions of dynamic and thermodynamic effects to the AR trend (b-c). (d-l) are similar to (a-c) but for GOGA2 (d-f), LENS2 (g-i), and PAC2 (j-l). Similarly, (d, g, j) are reproduced from Fig.5 (a, b, c) but shown in cylindrical map projection, respectively. Dots denote that the variables are statistically significant at the 95% confidence level according to the *t*-test for (a-c) and 1000-trail bootstrap resampling methods for (d-l), respectively. The red box in each subplot delineates the ABK region.

Supplementary Information for

Increased atmospheric rivers frequency slowed the seasonal recovery of the Arctic sea ice in recent decades

Pengfei Zhang[1*], Gang Chen[2], Mingfang Ting[3], L. Ruby Leung[4], Bin Guan[5,6], Laifang Li[1]

[1] Department of Meteorology and Atmospheric Science, The Pennsylvania State University, University Park, PA, USA
[2] Department of Atmospheric and Oceanic Sciences, University of California, Los Angeles, CA, USA
[3] Lamont-Doherty Earth Observatory, Columbia University, Palisades, NY, USA
[4] Atmospheric Sciences and Global Change Division, Pacific Northwest National Laboratory, Richland, WA, USA
[5] Joint Institute for Regional Earth System Science and Engineering, University of California, Los Angeles, CA, USA
[6] Jet Propulsion Laboratory, California Institute of Technology, Pasadena, CA, USA

Calculation of IVT

Reanalysis datasets: The daily wind and specific humidity at standard pressure levels below 200hPa are used to calculate the vertical integral of water vapor transport (IVT) for AR detection (Eq. 1). The integral of water vapor (IWV) is also calculated (Eq. 2).

$$\overrightarrow{IVT} = -\frac{1}{g}\int_{sfc}^{200hPa} \vec{V}\, qdp = -\frac{1}{g}\left(\int_{sfc}^{200hPa} uqdp + \int_{sfc}^{200hPa} vqdp\right) \quad (1)$$

$$\overrightarrow{IWV} = -\frac{1}{g}\int_{sfc}^{200hPa} qdp \quad (2)$$

Where g is the gravitational acceleration (m s^{-2}), q is the specific humidity (kg kg^{-1}), $\vec{V}$ is the wind vector (m s^{-1}) composed by zonal wind (u) and meridional wind (v), and p is the atmospheric pressure (hPa).

Model outputs: Due to the data availability, only the daily wind and specific humidity at the surface level, 850, 500, 200hPa are used in GOGA2 and PAC2. For LENS2, variables at the surface level, 850, 700, 500, 200hPa are available. There is almost no difference in the IVT calculation with or without the data at 700hPa, especially in the view of anomaly or trend. Thus, including 700hPa data in LENS2 does not impact the comparison between the ensembles in the view of the trend. At the grid where the bottom level is higher than 850hPa (and/or 700hPa for LENS2), i.e. the mountain regions, the values at the 850hPa (and/or 700hPa for LENS2) are excluded.

Sensitivity to the choice of AR detection threshold

In the polar regions, the choice of the AR detection threshold is region-dependent. For example, 98th percentile and 50 kg m^{-1} s^{-1} are used in different regions of the Antarctic (Wille et al. 2019; Francis et al. 2020), while the 150kg m^{-1} s^{-1} criterion is used in southern Greenland (Mattingly et al. 2018). In most regions of the Arctic, the absolute IVT threshold of 100 kg m^{-1} s^{-1} used in the current study is about 87-99th percentile in NDJ (FigS.3), indicating the IVT of a relative threshold varies largely in a relatively small region. We also checked the AR detection with relative thresholds, such as 90th, 95th, and even 98th percentile, shown in (FigS.1 d-f). In all three cases, the trend of AR frequency in the region of interest is significant and qualitatively consistent with that with the absolute threshold of 100 kg m^{-1} s^{-1}. Furthermore, using the original thresholds (85th percentile or 100 kg m^{-1} s^{-1}, whichever is greater) facilitates the discussion of the spatial pattern of AR changes involving the midlatitudes. Thus, we keep the 85th percentile or 100 kg m^{-1} s^{-1} for AR detection in this study.

Comparison between ARs, extreme transient transport, and moisture intrusion for the total Arctic moisture import

Previous studies have shown that the variability of the Arctic water vapor is driven by moisture transport, which is dominated by transient weather systems (89-94% at 70°*N*) (Rinke et al. 2009; Dufour et al. 2016), including moisture intrusion (Woods et al. 2013), extreme transient transport (Liu and Barnes 2015), and ARs (Nash et al. 2018). These weather systems including warm conveyor belts have overlapping features but by no means identical concepts of atmospheric flow

(Sodemann et al. 2020). The moisture intrusions, defined by using the vertical integral of meridional moisture transport (vq), the meridional component of Eq. 1, with a threshold of 200 Tg d^{-1} deg^{-1} (~90th percentile), account for 36% of the total poleward moisture transport across 70°N in winter (Woods et al. 2013). The extreme meridional transients ($v'q'$, where the prime denotes the deviation from the climatological mean) defined with a threshold of 90th percentile account for 38% of the total poleward transport across 70°N in winter and 32% in summer (Liu and Barnes 2015). In contrast, the ARs, usually identified using IVT (the complete form of Eq. 1), account for 70-80% of the total poleward moisture transport across 70°N (Nash et al. 2018). Here we confirm the climatological fractions at a range of high latitude-Arctic circles using ERA5 daily data as shown in Table S1. Although the values decrease along with the latitudes due to the low temperature, ARs still dominate the Arctic moisture import. The distinct portions of poleward moisture transports explained by moisture intrusion, extreme meridional transients, and ARs lie in their definitions. The moisture intrusion and extreme meridional transients are defined based on only the meridional component of IVT with a threshold of 90th percentile, and thus they preclude the strong poleward moisture transport with a relatively weak meridional component but a strong zonal component, i.e., the poleward moisture transport events tilting zonally. In fact, the latter is more common in mid-high latitude due to the prevailing westerly wind. Including all kinds of strong moisture transports, the median direction of ARs is ~60° in North Hemisphere and ~120° in South Hemisphere (0° = northward; 90° = eastward) (Guan and Waliser 2015), which is to say the strong poleward moisture transport events are more zonal than meridional. Given AR's definition is more representative of strong poleward moisture transport events, ARs could be regarded as the major weather system that drives the Arctic moisture imports (70-80% at 70°N, Nash et al. 2018), and therefore be used to explore the moisture-induced melting effect on the Arctic sea ice.

Quality and validation of reanalysis datasets

Despite the biases in magnitude, the spatial and temporal patterns of Arctic moisture transport in the reanalysis datasets show a remarkable agreement with the radiosondes (Dufour et al. 2016). Surface downward longwave radiation flux (DLW) in ERA5 is validated using satellite-derived data, Synoptic TOA and surface fluxes and clouds (SYN) version 4 from the Clouds and the Earth's Radiant Energy System (CERES) project (Doelling et al. 2016). CERES-SYN is available at a daily time scale at a 1°×1° resolution from March 2000 to the present. CERES-SYN is available from https://ceres.larc.nasa.gov/data/. Fig. S2 shows that the DLW in ERA5 agrees well with the satellite data, especially during the AR events in NDJ, suggesting the results related to DLW are reliable. Similar to radiation, rainfall and snowfall in ERA5 are also derived from the assimilation system of reanalysis. There is no long-period observation over the wide ocean for these two variables and thus they are hard to be validated. Generally, their reliability is relatively lower than commonly used variables, such as temperature, wind, et al, from the same reanalysis dataset. That is to say, the results related to rainfall could have unknown uncertainty, although intrinsic dynamical consistency exists among all variables in each reanalysis dataset.

Ice drift related to ARs

We estimate the anomalous SIA due to AR wind-induced ice drifting in ABK in NDJ based on NSIDC Polar Pathfinder Daily 25 km EASE-Grid Sea Ice Motion Vectors dataset (Tschudi et al. 2019), which is available from https://nsidc.org/data/NSIDC-0116. AR wind-induced ice drift in ABK is defined as the net ice drift across the ABK boundary when an AR is approaching or crossing the ice cover in ABK. The cumulated ice drift anomalies in NDJ associated with AR wind are smaller by 2-3 orders of magnitude compared to the AR-related SIA anomaly. The strong wind could change the ice distribution around the wind flow, such as SIC redistribution within a cyclone (Clancy et al. 2022), but change little the total SIA in a much larger region such as ABK. Thus, the big picture of ARs' impact on sea ice coverage lies in thermodynamic ice melting.

References for Supplementary Information:

Clancy, R., C. M. Bitz, E. Blanchard-Wrigglesworth, M. C. McGraw, and S. M. Cavallo, 2022: A cyclone-centered perspective on the drivers of asymmetric patterns in the atmosphere and sea ice during Arctic cyclones. *Journal of Climate*, **35**, 73–89, https://doi.org/10.1175/JCLI-D-21-0093.1.

Doelling, D. R., M. Sun, L. T. Nguyen, M. L. Nordeen, C. O. Haney, D. F. Keyes, and P. E. Mlynczak, 2016: Advances in Geostationary-Derived Longwave Fluxes for the CERES Synoptic (SYN1deg) Product. *Journal of Atmospheric and Oceanic Technology*, **33**, 503–521, https://doi.org/10.1175/JTECH-D-15-0147.1.

Dufour, A., O. Zolina, and S. K. Gulev, 2016: Atmospheric Moisture Transport to the Arctic: Assessment of Reanalyses and Analysis of Transport Components. *Journal of Climate*, **29**, 5061–5081, https://doi.org/10.1175/JCLI-D-15-0559.1.

Francis, D., K. S. Mattingly, M. Temimi, R. Massom, and P. Heil, 2020: On the crucial role of atmospheric rivers in the two major Weddell Polynya events in 1973 and 2017 in Antarctica. *Science Advances*, **6**, eabc2695, https://doi.org/10.1126/sciadv.abc2695.

Guan, B., and D. E. Waliser, 2015: Detection of atmospheric rivers: Evaluation and application of an algorithm for global studies. *J. Geophys. Res.*, **120**, 12514–12535, https://doi.org/10.1002/2015jd024257.

Liu, C., and E. A. Barnes, 2015: Extreme moisture transport into the Arctic linked to Rossby wave breaking. *J. Geophys. Res.*, **120**, 2014JD022796, https://doi.org/10.1002/2014JD022796.

Mattingly, K. S., T. L. Mote, and X. Fettweis, 2018: Atmospheric River Impacts on Greenland Ice Sheet Surface Mass Balance. *Journal of Geophysical Research: Atmospheres*, **123**, 8538–8560, https://doi.org/10.1029/2018JD028714.

Nash, D., D. Waliser, B. Guan, H. Ye, and F. M. Ralph, 2018: The Role of Atmospheric Rivers in Extratropical and Polar Hydroclimate. *Journal of Geophysical Research: Atmospheres*, **123**, 6804–6821, https://doi.org/10.1029/2017JD028130.

Rinke, A., C. Melsheimer, K. Dethloff, and G. Heygster, 2009: Arctic Total Water Vapor: Comparison of Regional Climate Simulations with Observations, and Simulated Decadal

Trends. *Journal of Hydrometeorology*, **10**, 113–129, https://doi.org/10.1175/2008JHM970.1.

Sodemann, H., and Coauthors, 2020: Structure, Process, and Mechanism. *Atmospheric Rivers*, Springer, p. 252.

Tschudi, M., W. N. Meier, J. S. Stewart, C. Fowler, and J. Maslanik, 2019: *Polar Pathfinder Daily 25 km EASE-Grid Sea Ice Motion Vectors, Version 4*. NASA National Snow and Ice Data Center Distributed Active Archive Center, https://doi.org/10.5067/INAWUWO7QH7B.

Wille, J. D., V. Favier, A. Dufour, I. V. Gorodetskaya, J. Turner, C. Agosta, and F. Codron, 2019: West Antarctic surface melt triggered by atmospheric rivers. *Nature Geoscience*, **12**, 911–916, https://doi.org/10.1038/s41561-019-0460-1.

Woods, C., R. Caballero, and G. Svensson, 2013: Large-scale circulation associated with moisture intrusions into the Arctic during winter. *Geophysical Research Letters*, **40**, 4717–4721, https://doi.org/10.1002/grl.50912.

Supplementary Figures

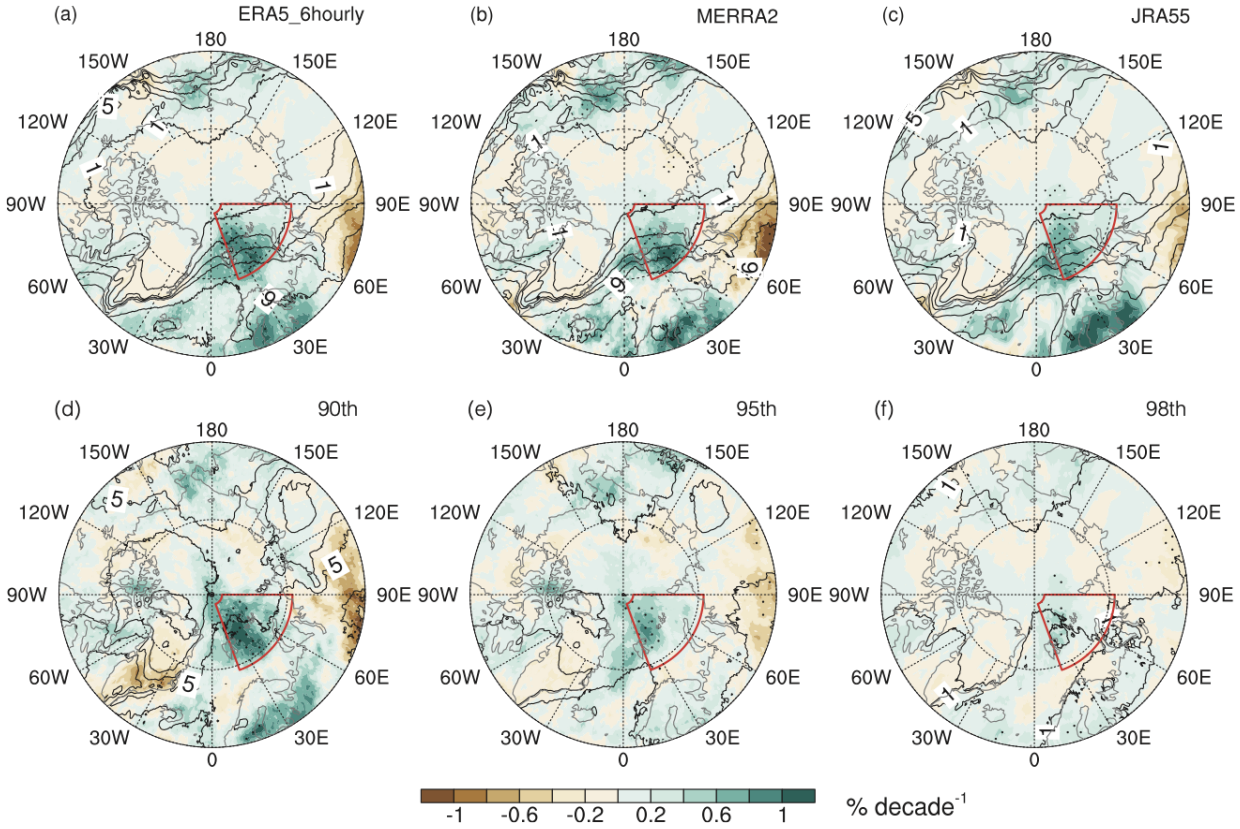

Fig.S1 Observed AR frequency trend similar to Fig. 2a but with ERA5 6 hourly data (a), MERRA2 daily data (b), JRA55 daily data (c). (d-f) same as Fig2.a but the ARs are detected using 90th (d), 95th (e), and 98th (f) percentile. The red box in each panel highlights the region of interest.

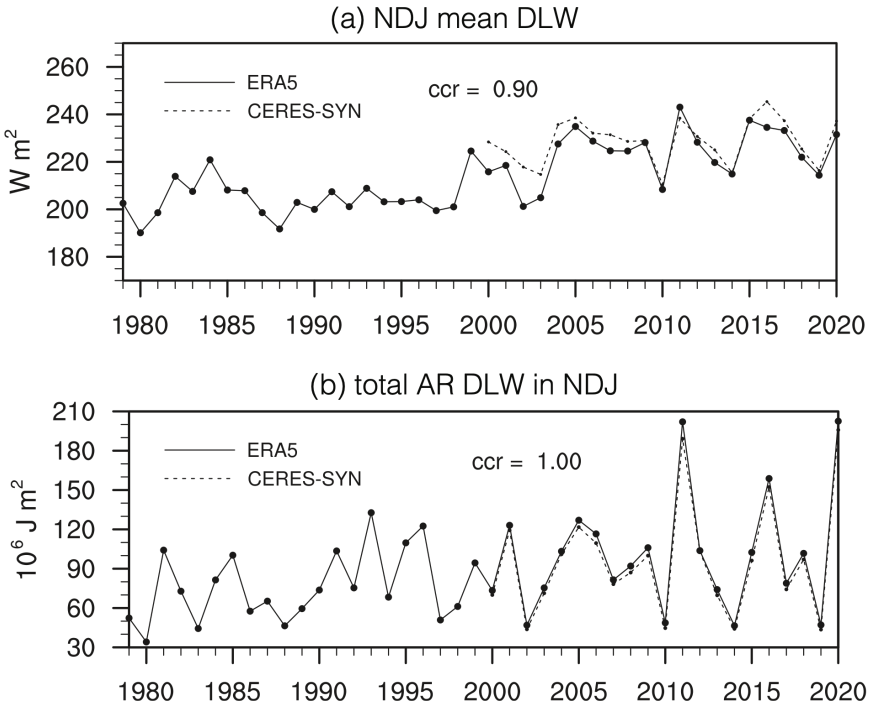

Fig.S2 Validation of downward longwave radiation at the surface (DLW) in ERA5. (a) Time series of NDJ mean DLW (W m^{-2}) in ABK area in reanalysis dataset ERA5 in 1979-2020 (solid) and satellite observation CERES-SYN (dashed) in 2000-2020. The digits denote the correlation coefficient between these two time series during the period of 2000-2020. (b) Same as (a) but for AR-induced total longwave radiation (10^6 J m^{-2}) in NDJ. Note that the values in (b) are the results of integration over time (Method), and thus the units are different in these two panels. The DLW in ERA5 has a remarkable agreement with satellite observation, especially during the AR activities.

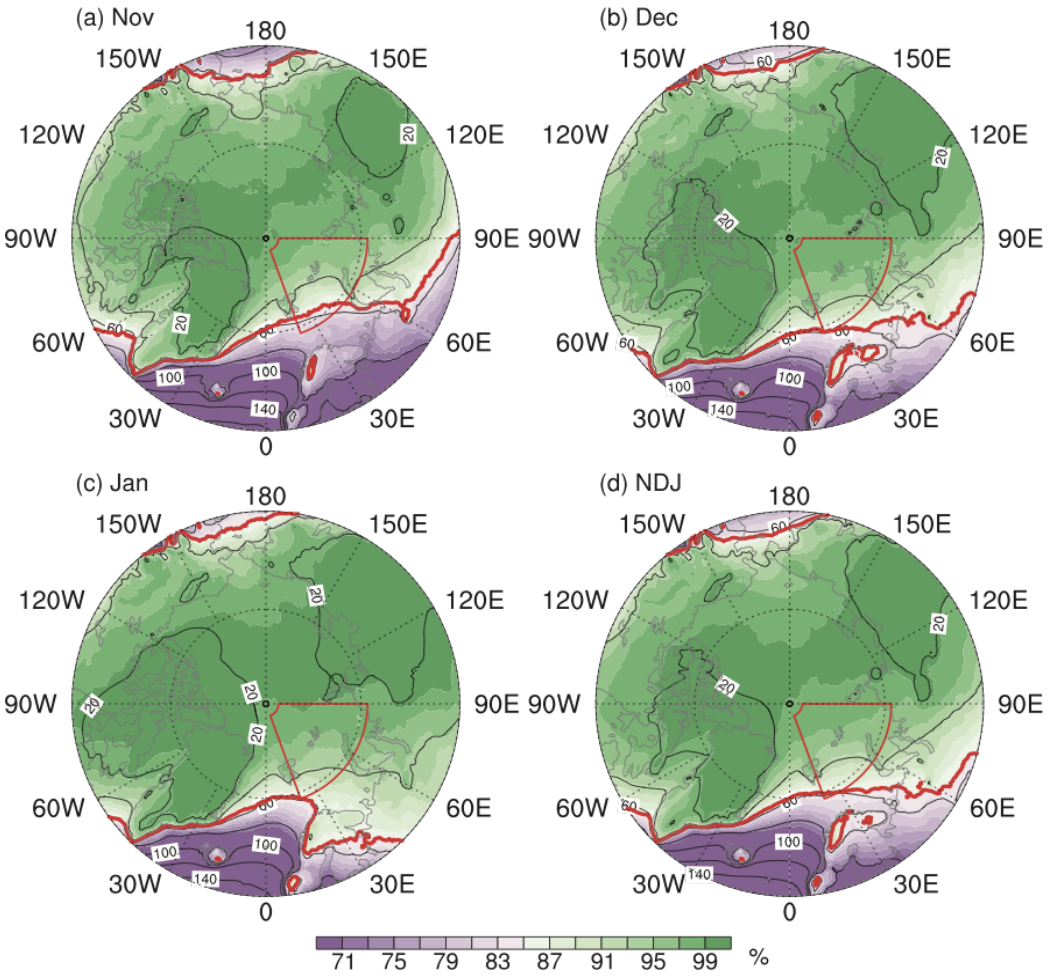

Fig.S3 Percentile of 100 kg m^{-1} s^{-1} IVT in Nov, Dec, Jan, and whole NDJ. Black contours show the climatology of IVT. The red thick line in each subplot highlights the 85th percentile contour of 100 kg m^{-1} s^{-1} IVT.

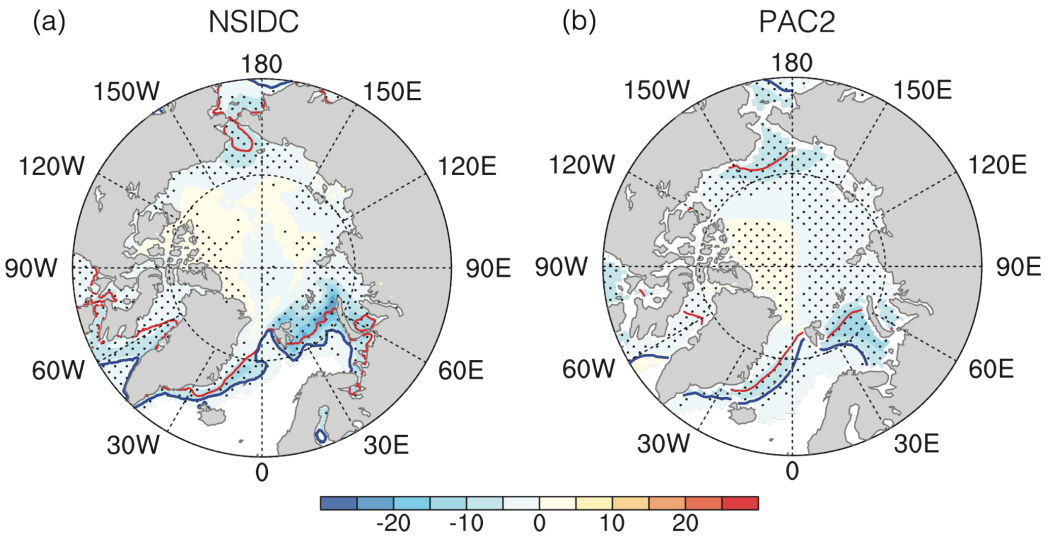

Fig.S4 Trends in sea ice concentration (SIC) in NDJ in recent decades. (a) Trend in 1979-2020 in NSIDC. (b) Trend in 1979-2013 in the model ensemble from PAC2. Unit is % decade^{-1}.

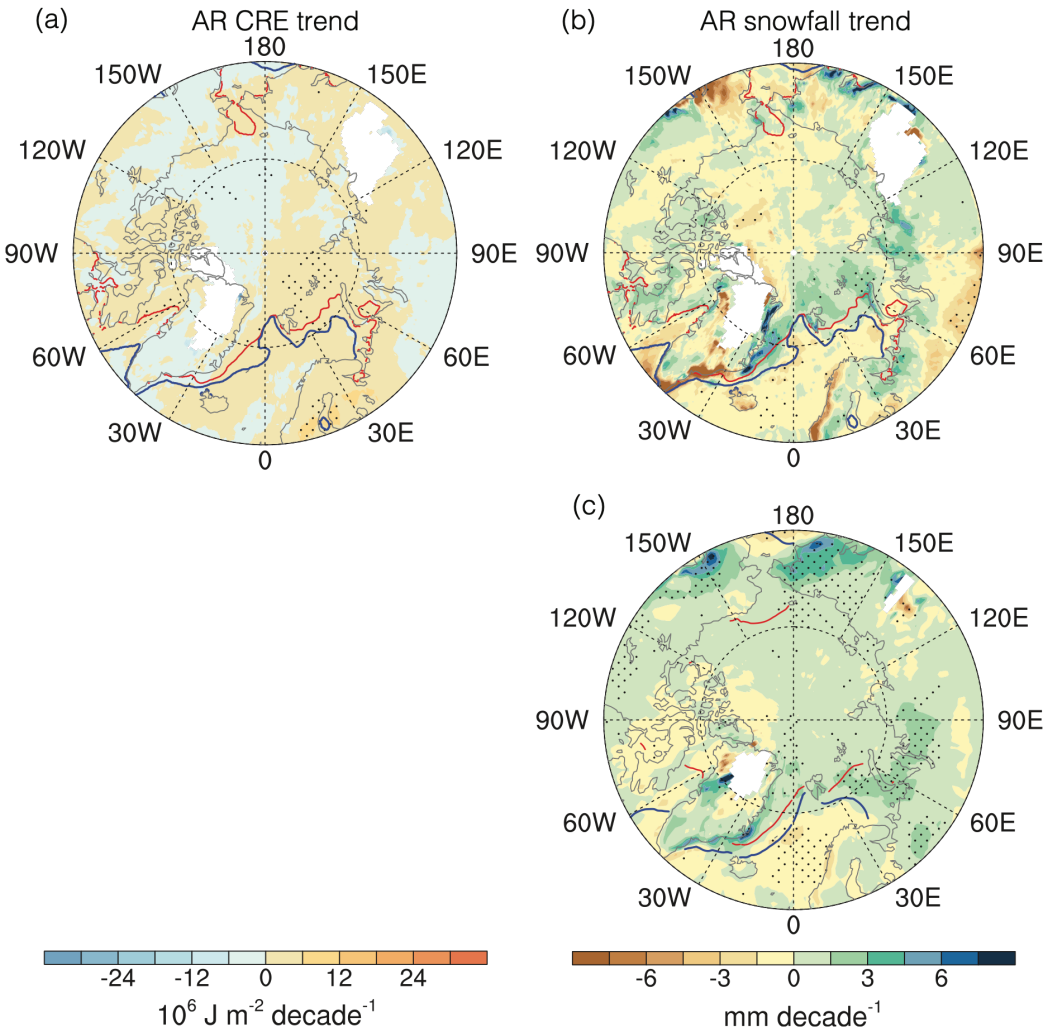

Fig.S5 AR-induced trends in cloud radiative effect in cumulated DLW (left) and snowfall (right) in NDJ in ERA5 (a,b) and the model ensemble from PAC2 (c). See Method for the calculation details of the total amounts of the flux variables associated with ARs in NDJ. The cloud radiative effect of DLW is expressed as the difference between DLW and clear sky DLW. The cloud radiative effect of longwave radiation in PAC2 is missing due to no clear sky DLW output in PAC2.

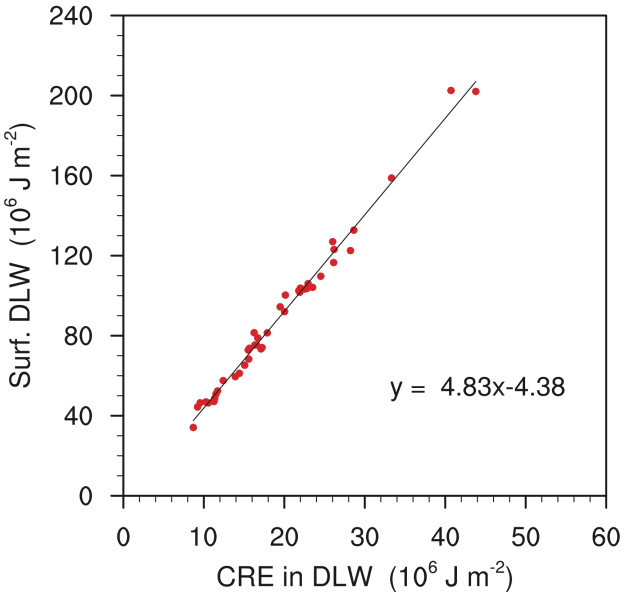

Fig.S6 Proportional contribution of cloud radiative effect to the cumulated surface DLW related to ARs in NDJ in 1979-2020 in ERA5. The linear fit is shown as the black line and the equation.

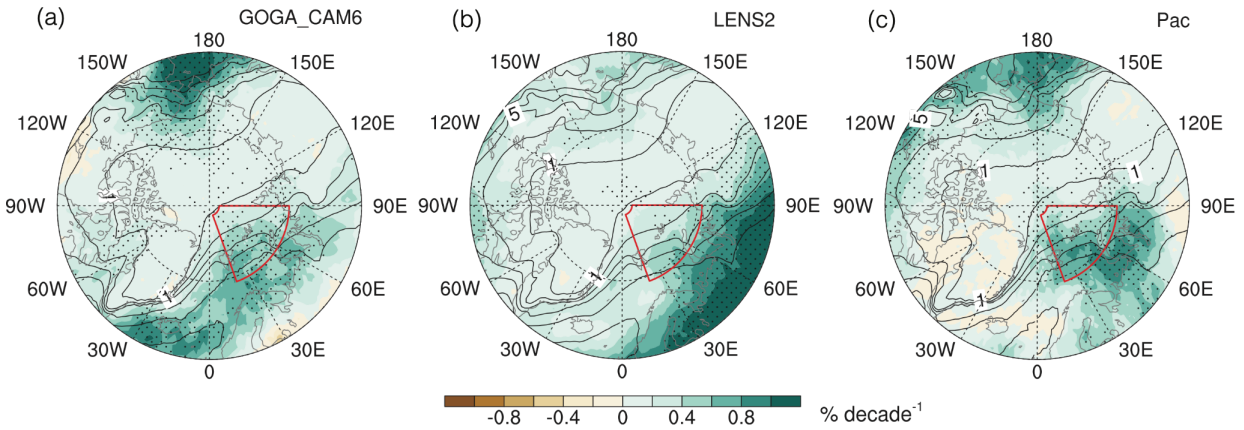

Fig.S7 Agreement for the sign of the AR changes among members in each ensemble. (a-c) the same as Fig.5(a-c) but the dots denote >80% agreement among ensemble members.

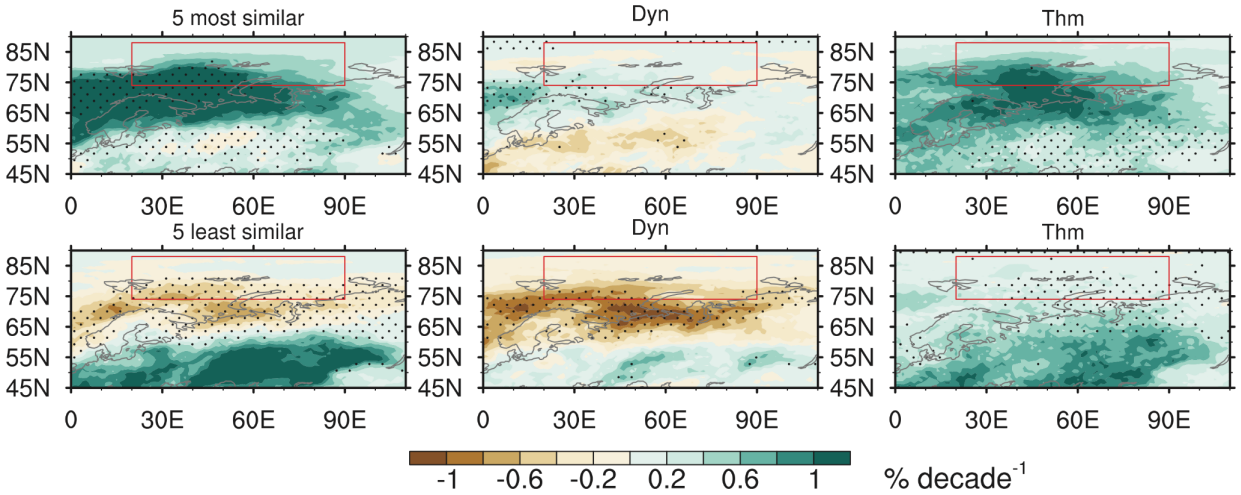

Fig.S8 AR frequency trend in selected individual members in LENS2. The left column shows the mean AR frequency trend in 5 LENS2 members who are most (least) similar to GOGA2 in the area of (0°-110°*E*, 45°-90°*N*). Here, we regard the AR trend pattern in GOGA2 as the reference pattern considering the system consistency. The results are similar for using PAC2 as the reference pattern. The middle and right columns are the contributions of dynamic and thermodynamic effects, similar to that in Fig.6. The dots indicate the AR changes are significantly different from the other 45 members in LENS2 using the 1000 times bootstrap resampling methods. The results are similar in the composites of the LENS2 sub-ensembles with the largest (smallest) trends in ABK, which we have confirmed.

Supplementary tables

Table S1 Fraction of mean annual total poleward IVT explained by ARs in ERA5 in 1979-2021

60°*N*	65°*N*	70°*N*	75°*N*	80°*N*
81%	78%	75%	71%	69%